Fan Fei
Department of Industrial and Systems Engineering,
Iowa Technology Institute,
University of Iowa,
Iowa City, IA 52242
e-mail: fan-fei@uiowa.edu

Li He
Department of Industrial and Systems Engineering,
Iowa Technology Institute,
University of Iowa,
Iowa City, IA 52242
e-mail: li-he@uiowa.edu

Levi Kirby
Department of Industrial and Systems Engineering,
Iowa Technology Institute,
University of Iowa,
Iowa City, IA 52242
e-mail: levi-kirby@uiowa.edu

Xuan Song[1]
Department of Industrial and Systems Engineering,
Iowa Technology Institute,
University of Iowa,
Iowa City, IA 52242
e-mail: xuan-song@uiowa.edu

Study of Droplet Diffusion in Hydrothermal-Assisted Transient Jet Fusion of Ceramics

Hydrothermal-assisted transient jet fusion (HTJF) is a powder-based additive manufacturing (AM) method of ceramics, which utilizes a water-mediated hydrothermal mechanism to fuse particles together, eliminating the use of organic binders in forming green bodies and thereby contributing to high green-density parts (>90%) advantageous for fabricating functional materials with high performance. In the HTJF process, a transient solution such as water is selectively deposited into a powder bed in a layer-by-layer fashion followed by a hydrothermal fusion process. Upon the ejection and deposition of a droplet of the transient solution on the surface of the powder bed, the diffusion behavior of the liquid significantly influences the particle fusion and the fabrication accuracy of the HTJF process. Precise control of the liquid diffusion in the powder bed is critical for the fabrication of ceramic structures with both high density and accuracy. In this paper, the dependence of transient solution diffusion on different process parameters (i.e., powder packing density, droplet size, pressure, etc.) in the HTJF process were studied. Both numerical modeling and experimental methods were used to quantify the relationships between processing parameters and diffusion profiles of transient solution droplets (e.g., diffusion width/depth). Optimum processing conditions were identified to mitigate the undesired diffusion of transient solution droplets in the powder bed. [DOI: 10.1115/1.4048444]

Keywords: hydrothermal-assisted transient jet fusion, green density, diffusion profile, additive manufacturing, transient solution, modeling and simulation, powder processing

1 Introduction

In nature, rocks are formed through a natural lithification process [1], in which particle sediments are rearranged by the compaction from the intense pressing weight of overlying sediments, and are finally cemented together when water with dissolved minerals flow into the empty spaces of particle sediments and crystalized the spaces with new minerals. The lithification process of rocks only requires mild temperature and pressure, along with groundwater to bond particles together. Inspired by this natural process, a new additive manufacturing (AM) method, named *hydrothermal-assisted transient jet fusion* (HTJF), has been developed in our prior work to obviate the need for a large amount of organic binders in ceramic AM [2].

1.1 Introduction to the HTJF Process. Figures 1(*a*)–1(*c*) show the primary fabrication procedures of the HTJF process, including transient solution deposition, hydrothermal fusion, and de-powdering: (1) in transient solution deposition (refer to Fig. 1(*a*)), a transient solution (such as water) is selectively deposited into a ceramic nano-powder bed via an inkjet printhead in a layer-by-layer fashion; the packing density of each layer of powder is adjusted by manually pressing the layer prior to the liquid deposition. (2) After a powder compact with selectively deposited water is achieved, a hydrothermal condition (including a low heating temperature and a uniaxial pressure) is applied to the powder bed to trigger the nanoparticle fusion in the water-deposited region, as shown in Fig. 1(*b*). In our process, the temperature is controlled by a thermal resistor, a thermocouple, and a PID controller, and the uniaxial pressure is applied by an embedded piston and a load cell mounted under the powder platform. (3) Following that, a de-powdering process is performed to remove the unfused, loose nanoparticles from the hydrothermally processed powder compact, leaving only the fused ones (the so-called green part) to be further sintered (refer to Fig. 1(*c*)). It should be noted that during the HTJF fabrication process, two types of pressing have been applied, including the manual pressing of each layer for adjusting powder packing density in step (1) and the hydrothermal pressing for triggering particle fusion in step (2). In this paper, we refer to the former one as pre-press and the latter one as final press.

The basic fusion mechanism behind the HTJF process is illustrated in Figs. 1(*d*)–1(*i*). Once deposited on the powder bed, a water droplet rapidly diffuses through the porous powder bed under gravity and capillary pressure and meanwhile starts to dissolve the surface of each nanoparticle, as depicted in Figs. 1(*d*)–1(*g*). As a heating temperature and a uniaxial pressure are simultaneously applied to the powder bed (refer to Fig. 1(*e*)), nanoparticles move into contact with each other, and the deposited water continues to diffuse, resulting in full saturation or occupation of water in interparticle pores. Due to the large difference in chemical potential, the dissolved species in the deposited water tends to move from the contact areas of nanoparticles (high chemical potential) toward the pores (low chemical potential) through the water flow (refer to Fig. 1(*h*)). The dissolved species finally precipitates on the nanoparticle surfaces away from the contact areas after the water evaporates, resulting in the fusion of two neighboring nanoparticles (see Figs. 1(*f*)–1(*i*)). Based on this fusion mechanism, the HTJF method can not only process ceramic powders with (partial) solubility in water or volatile solutions such as lithium molybdate (Li_2MoO_4), vanadium oxide (V_2O_5), zirconia (ZrO_2), etc. [3–5] but can also be applicable to ceramics with incongruent dissolution (e.g., barium titanate, $BaTiO_3$) by incorporating hydrothermal precursor

[1]Corresponding author.

Manuscript received May 18, 2020; final manuscript received May 28, 2020; published online November 10, 2020. Assoc. Editor: Y. Lawrence Yao.

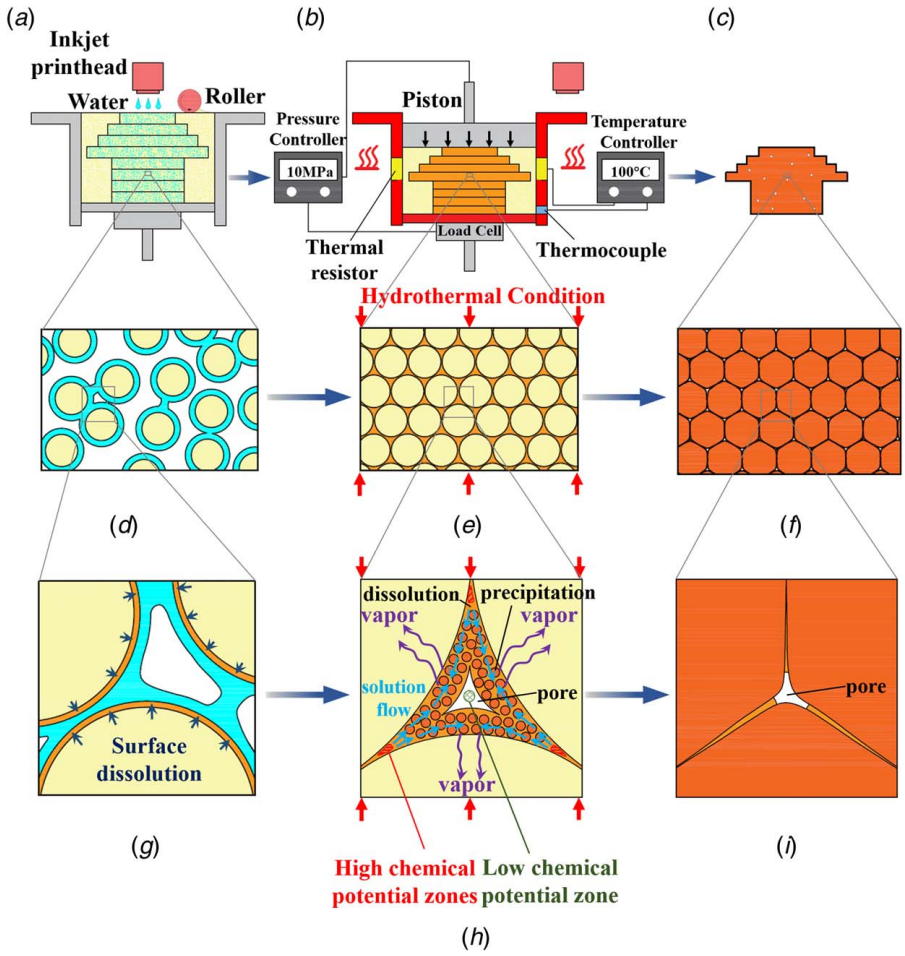

Fig. 1 Schematics of the HTJF process

solutions as have been used in extensive hydrothermal syntheses studies and cold sintering [3,6–9].

Compared with other AM processes of ceramics, such as indirect selective laser sintering (SLS) [10,11], stereolithography (SL) [12–14], and binder jetting (BJ) [9,15,16], a key benefit of the HTJF process lies in the capability of achieving high green density by eliminating the use of organic binders. Those existing ceramic AM processes typically use a high volume fraction of binders for shaping green parts (e.g., up to 70 vol% of a photopolymer resin used in ceramic SL processes), which leads to a relatively lower final density than that of their traditionally manufactured counterparts. In the HTJF process, since few or even no organic binder is used, a pure green body with a density greater than 90% can be achieved [2].

1.2 Objectives. The diffusion of a transient solution in a powder bed plays a significant role in controlling the fusion profiles in the HTJF process. Based on the order of their occurrence, we classify the diffusion phenomena in the HTJF process into three categories, including passive diffusion, rearrangement diffusion, and hydrothermal diffusion. Passive diffusion occurs under the effects of gravity and capillary forces upon the deposition of the transient solution into the powder bed, which is determined by the size and distribution of pores in the powder bed. Similar diffusion behaviors also occur in many other AM processes, such as binder jetting [17–19], electrochemical additive manufacturing [20], and SLM [21]. Rearrangement diffusion is caused by the particle rearrangement under an applied pressure (via final press in the procedure of hydrothermal fusion), which pushes the particles and surrounding liquid to an equilibrium position. Hydrothermal diffusion is driven by an enhanced capillary force after a stabilized hydrothermal condition is established (e.g., no nanoparticle movement), which facilitates the mass transport and precipitation of dissolved materials into the pores.

In the HTJF process, both passive diffusion and rearrangement diffusion influence the distribution of a transient solution in the powder bed prior to the start of the hydrothermal fusion of nanoparticles, which consequently influences the accuracy of fabrication results. A bad control of these two diffusion behaviors leads to undesired fusion in final parts. For example, Fig. 2 shows the influence of diffusion on two samples fabricated by the HTJF process. Comparing with the computer-aided design (CAD) models of cross shape and "I" letter shape shown in Figs. 2(*a*)–2(*c*), overcuring can be seen in the corresponding fabrication results shown in Figs. 2(*b*) and 2(*d*) [2].

The research objectives of this paper are to study the effects of different process parameters (i.e., powder packing density, droplet size, pressure, etc.) on transient solution diffusion in particular passive diffusion and rearrangement diffusion in the HTJF process and to identify optimum processing conditions to mitigate the undesired overcuring in final parts. Our hypothesis is that, by optimizing the packing density and the final press, the passive and rearrangement diffusion can be controlled, and the overcuring problem can be solved. In this work, the diffusion behavior of a transient solution in the HTJF process was studied by modeling and measuring the diffusion profiles of sessile droplets in a powder bed. The rest of this paper is organized as follows. Section 2 presents both numerical modeling and experimental methods to quantify the relationships between processing parameters and diffusion profiles of transient solution droplets (e.g., diffusion width/depth). More specifically, the materials used in the experiments are introduced; the governing equations for the diffusion of a sessile-droplet

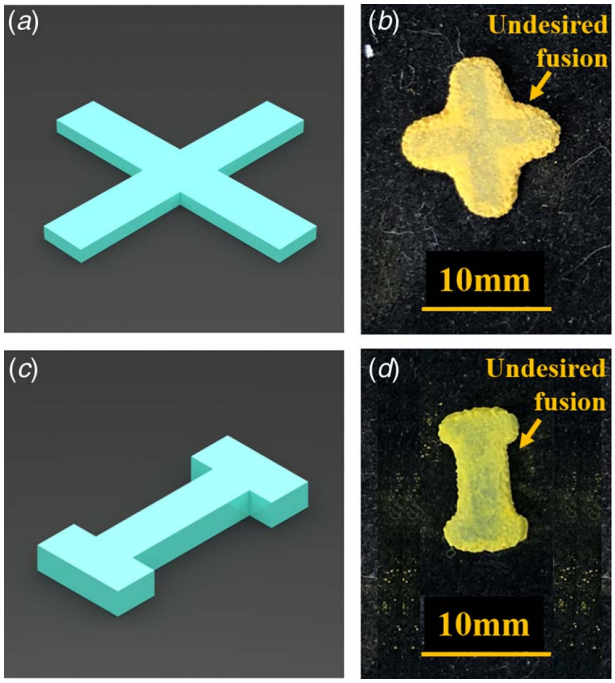

Fig. 2 Diffusion problem in the HTJF process: (*a*) a CAD model of a cross shape, (*b*) a fabricated sample of a cross shape, (c) a CAD model of "I" letter shape, and (*d*) a fabricated sample of "I" letter shape

model are discussed; and a numerical model of droplet diffusion in porous media using ANSYS FLUENT is presented. Experiments on diffusion of sessile droplets in a powder bed were conducted by varying droplet sizes, powder's packing density, and final pressure. Section 3 presents the simulation and experimental results. Section 4 makes the conclusions and recommendations for controlling droplet diffusion in a powder bed, which is valuable to improve the accuracy of fabrication in the HTJF process.

2 Materials and Methods

2.1 Materials. In the present work, lithium molybdate (Li_2MoO_4, 99+%, Alfa Aesar, Haverhill, MA) was used as a model material, which is an inorganic compound widely applied in antennas due to its low loss dielectric properties [22,23]. Lithium molybdate is a white, odorless powder, as shown in Fig. 3(*a*). The material is very soluble in water and has a melting point of 705 °C. The used particle size is around 1 μm with a roughly spherical shape, as shown in Fig. 3(*b*). Because of its high solubility in water and spherical shape, lithium molybdate is a suitable material for the HTJF process and was hence used to study typical diffusion profiles of water in a powder bed.

To study the diffusion profile of a transient solution, a water-based solution has been synthesized, whose components are

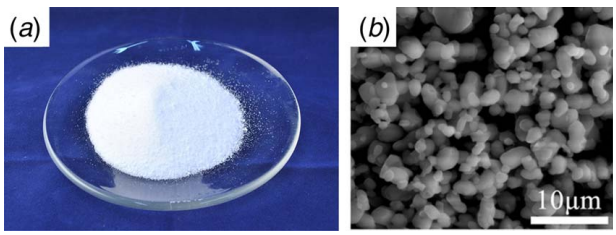

Fig. 3 Lithium molybdate used in the HTJF process: (*a*) as-received powder and (*b*) particles in scanning electron microscope (SEM)

Table 1 Components and corresponding weight percent of transient solution used in experiments

Components	wt%
Water	60
Ethanol	36
Poly(vinyl alcohol) (PVA)	2
Propylene glycol	2

shown in Table 1. Since the focus of this paper is on the passive and rearrangement diffusion, we decoupled the effects of hydrothermal diffusion on the diffusion profile by using a room temperature in the procedure of hydrothermal fusion. PVA and propylene glycol were thereby added to enhance the strength of achieved granules for diffusion profile measurements. Ethanol was added to reduce the solution's viscosity for inkjet printing in the HTJF process.

2.2 Governing Equations and Numerical Model. Inkjet printing of water into a powder bed can be seen as a sessile-droplet model, as shown in Fig. 4. The governing equations used in numerical modeling follow the Navier–Stokes equations. We assume that the liquid and gas in the HTJF process are incompressible and Newtonian and have constant properties together with laminar fluid flow [24]. The mass and momentum equations of the fluid are shown in Eqs. (1) and (2):

$$\nabla \cdot \mathbf{V} = 0 \tag{1}$$

$$\rho\left(\frac{\partial \mathbf{V}}{\partial t} + \mathbf{V} \cdot \nabla \mathbf{V}\right) = -\nabla p + \nabla[\mu(\nabla \mathbf{V} + \nabla \mathbf{V}^T)] + \sigma\kappa\delta_s\mathbf{n} \tag{2}$$

where ρ is the density of fluid, μ is the viscosity of fluid, $\mathbf{V}$ is the velocity vector, and p is the pressure. $\sigma\kappa\delta_s\mathbf{n}$ is the surface tension force concentrated at the interface, where δ_s is Dirac distribution function, σ is surface tension coefficient, κ and $\mathbf{n}$ are the curvature and the unit normal vector of the interface [25,26].

A volume of fluid (VOF) method was used to track the interface between fluid and air phases [27]. Using the VOF method, density ρ and viscosity μ in each computational grid are dependent on volume fraction of fluid α as follows:

$$\rho = \alpha\rho_{liquid} + (1-\alpha)\rho_{gas} \tag{3}$$

$$\mu = \alpha\mu_{liquid} + (1-\alpha)\mu_{gas} \tag{4}$$

where $\alpha = 1$ represents liquid in the computational grid, $\alpha = 0$ represents gas in the computational grid, and $0 < \alpha < 1$ represents that the grid contains a mixture of liquid and gas.

In order to simulate the diffusion of a droplet in a powder bed, a model geometry was designed in ANSYS FLUENT as shown in Fig. 5,

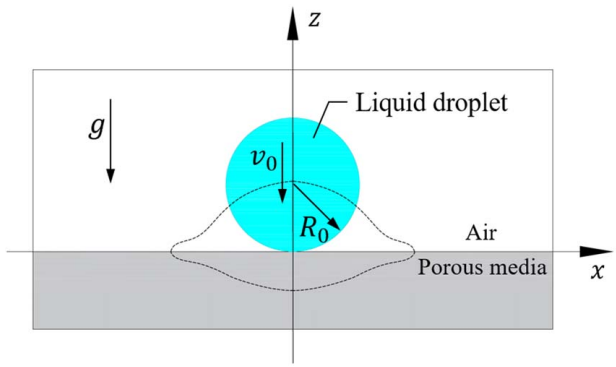

Fig. 4 Droplet diffusion in a powder bed

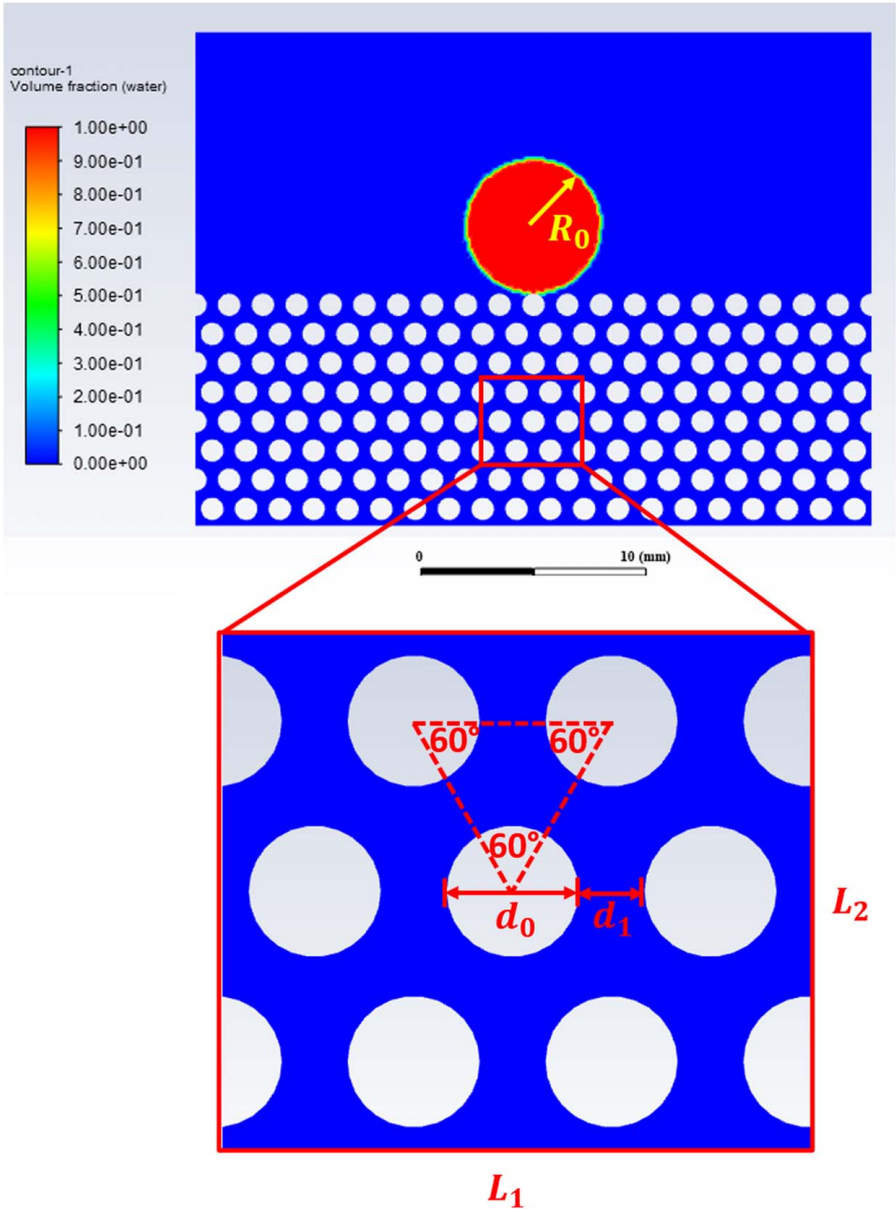

Fig. 5 The model geometry used in ANSYS FLUENT

in which the powder bed is composed of particles with a diameter of d_0 and the distance between the particles is d_1. The droplet, which is the larger circle on the top , has a radius of R_0. The heat map represents the volume fraction of liquid (0∼1). The packing density was calculated based on a rectangular area A of nanoparticles with a length of L_1 and a width of L_2, as shown in the inset in Fig. 5. L_1 and L_2 can be written as

$$L_1 = 3(d_0 + d_1) \tag{5}$$

$$L_2 = \frac{3\sqrt{3}}{2}(d_0 + d_1) \tag{6}$$

The area of the rectangle A is

$$A = L_1 L_2 = \frac{9\sqrt{3}}{2}(d_0 + d_1)^2 \tag{7}$$

The total area A_p of all the nanoparticles in the rectangle A is

$$A_p = \frac{9}{4}\pi d_0^2 \tag{8}$$

Then, the packing density ρ_p of particles in this rectangular area can be calculated by

$$\rho_p = \frac{A_p}{A} = \frac{\sqrt{3}\pi}{6}\left(\frac{d_0}{d_0 + d_1}\right)^2 \tag{9}$$

Based on Eq. (9), the distance between the particles can be written as

$$d_1 = d_0(0.952\rho_p^{-1/2} - 1) \tag{10}$$

Given a certain packing density of a powder bed, Eq. (10) was used to calculate d_1 for the powder bed model in the simulation. Since transient solutions used in the HTJF process contain a high volume fraction of water, the properties of water were used in the simulation. All materials properties used in the simulation for water, air, and particles are listed in Table 2.

Table 2 Properties of water, air, and particles used in ANSYS FLUENT

Parameter	Value
Density of liquid (kg/m^3)	998.2
Viscosity of liquid (kg/m·s)	0.001003
Surface tension coefficient (N/m)	0.03
Contact angles between particle-water and air (deg)	65
Initial velocity of droplet in vertical direction (m/s)	−0.05
Gravity (m/s^2)	−9.81

2.3 Experimental Investigation

2.3.1 Measurement of Diffusion Profiles. In order to establish the relationship between the diffusion profile of a transient solution in a powder bed and the process parameters such as powder packing density, final press, and droplet size, an experimental setup was built as shown in Fig. 6(*a*), which comprised a powder reservoir containing a small powder bed of Li_2MoO_4 and a support frame holding a syringe at a certain height. The end of the syringe was connected to a dispensing nozzle with a certain diameter. The droplet size from the nozzle was always measured prior to testing. Figure 6(*a*, 2) shows an example of a droplet deposited from a nozzle with an inner diameter of 1.2 mm. The diameter of the formed droplet was measured as 2.25 mm.

For each group of process parameters, the packing density of the powder bed was first adjusted by pre-pressing with a given pressure, as shown in Fig. 6(*a*, 1). Three droplets were then individually deposited into the pre-pressed powder bed (refer to Fig. 6(*b*)). After all the droplets penetrated through the powder bed, the powder bed was pressed under a certain final pressure, as shown in Fig. 6(*c*). The powder compact was finally dried in an oven at 120 °C for 3 h, which bonded the powders containing the diffused droplet into a granule. The dry powders around the bonded granule were loose and were manually removed by a needle. After removing the dry powders, the geometry (height/width) of the leftover, bonded granule was then measured to approximate the diffusion profile of the solution droplet.

2.3.2 Investigation on the Effects of Droplet Depositing Strategy. In transient solution deposition (Fig. 1(*a*)), the same amount of water can be delivered into a powder bed by depositing a large droplet for once or multiple smaller droplets sequentially. How the droplet depositing strategy of droplet size and dropping interval influences the diffusion profile in a powder bed remains unknown. In order to study that, three nozzle sizes were used, as shown in Fig. 7.

Table 3 shows the droplet size formed by each nozzle. Average diameters of the droplets were measured from the images (Fig. 7).

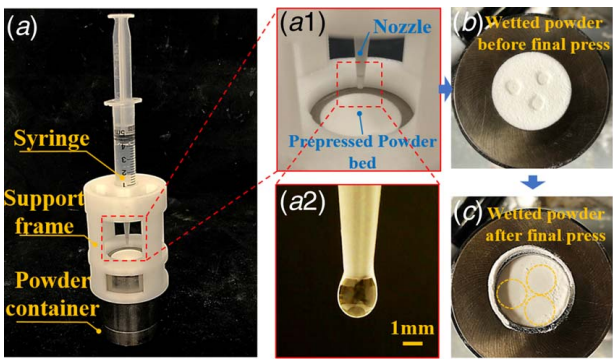

Fig. 6 Experiment procedures: (*a*) experiment setup, (*a*1–*a*2) details of the setup, (*b*) three droplets deposited into the pre-pressed powder bed, and (c) the powder bed after final press for diffusion measurements

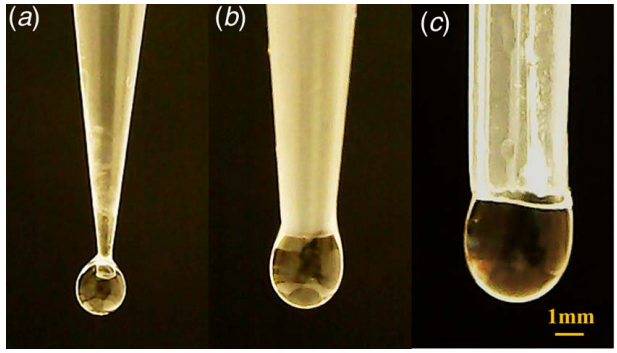

Fig. 7 Droplets formed from nozzles with inner diameters of (*a*) 0.20 mm, (*b*) 1.2 mm, and (c) 2.4 mm

Table 3 Measurement results of droplets

Nozzle	Inner diameter (mm)	Droplet diameter (mm)	Droplet volume (mm^3)	Volume ratio relative to nozzle a
a	0.2	1.55	1.95	1
b	1.2	2.25	5.96	3
c	2.4	3.33	19.32	10

As given in the table, the droplet volume achieved by Nozzle b is three times as that of nozzle a, and the droplet volume by nozzle c is 10 times as that of nozzle a. Based on the volume ratio, nozzle a was selected to deposit small droplets with a diameter of 1.55 mm, and nozzle b was used to deposit larger droplets with a diameter of 2.25 mm. To deliver the same amount of water, two droplet depositing strategies are available. Strategy a is to drop multiple small droplet separately with certain interval between each dropping; strategy b is to drop one large droplet individually. Nozzle a used the dropping strategy (strategy a) of dropping three droplets sequentially (~2 s interval between each droplet) onto the same spot in the powder bed, and nozzle b used the strategy (strategy b) of dropping one droplet for once. The height of the droplets from those two nozzles to the powder bed was fixed at 10 mm. The depth and width of the diffusion profiles resulting from both strategies were measured. The measurement accuracy of the droplet volumes can be further improved in the future by indirectly measuring the weight of each droplet and density of the solution.

2.3.3 Investigation on the Effects of Powder Packing Density. To study the effects of the packing density of a powder bed on the diffusion profile, different powder packing densities were achieved by pre-pressing the powder bed via a hydraulic press machine with different pressures (i.e., 0–12.49 MPa) under room temperature prior to depositing a droplet. The powder bed's volume prior to pressing was premeasured based on the volume of the powder container. The powder bed without pre-press was formed by carefully filling the powder container (in Fig. 6(*a*)) and flattening the top surface using a doctor blade. As a result, the packing density of the powder bed is influenced only by the pre-press applied. Vibration was avoided during the test to prevent unrelated factors from influencing the calculated density. The moving distances of the pressing piston were measured. The packing density of the powder bed can be calculated by Eq. (11)

$$\rho_p = \frac{m}{V} = \frac{m}{\frac{1}{4}\pi d_c^2 (h_0 - \Delta h)} \tag{11}$$

where d_c is the diameter of the powder container, h_0 is the initial height of the powder bed, and Δh is the moving distance of the

powder bed after pre-press. A relationship between the applied pre-pressing pressure and the resulting powder packing density was established.

2.3.4 Investigation on the Effects of Final Press. As explained in Sec. 1, rearrangement diffusion of a droplet in the HTJF process is mainly determined by the relative movement of particles under the effect of final press. We hypothesize that a smaller difference between final press and pre-press will result in less diffusion of droplets. To test this hypothesis, three final pressures (including 0 MPa, 6.25 MPa, and 12.49 MPa) were applied under room temperature to the powder bed which was first pre-pressed at different pressures (0–12.49 MPa). The resulting diffusion profiles were measured and compared for different pressure differences.

2.3.5 Test Case Fabrication via HTJF. Guided by the relationship between the diffusion profiles and pre-press/final press, different combinations of pre-press and final press were selected and applied to the HTJF process for actual printing. The samples printed under different pre-press and final press were compared with verify the effectiveness of diffusion control during the fabrication process.

3 Results and Discussion

3.1 Relationship Between Packing Density and Pre-press Pressure. The packing density of a powder bed can be varied by applying different pre-press pressures to it [28,29]. Pre-press was applied to the powder bed by a hydraulic press machine to vary the density of the powder bed (Fig. 8(*a*)). The effect of pre-press on powder packing density is given in Fig. 8(*b*). As the pre-press pressure increased from 0 to 3.12 MPa, the packing density increased dramatically from 54.4% to 71.49%. This increase is easy to understand in that the applied pre-press pushed the powder particles closer to each other resulting in a decreased porosity in the powder bed. When the pre-press further increased above 3.12 MPa, the packing density reached a plateau where the packing density only increased by 1.48% when pre-press increased from 3.12 MPa to 12.49 MPa. This indicates that beyond the pre-press pressure of 3.12 MPa, a tighter packing configuration was obtained, and sufficient particle–particle contacts were generated that prevented particle movement and rearrangement.

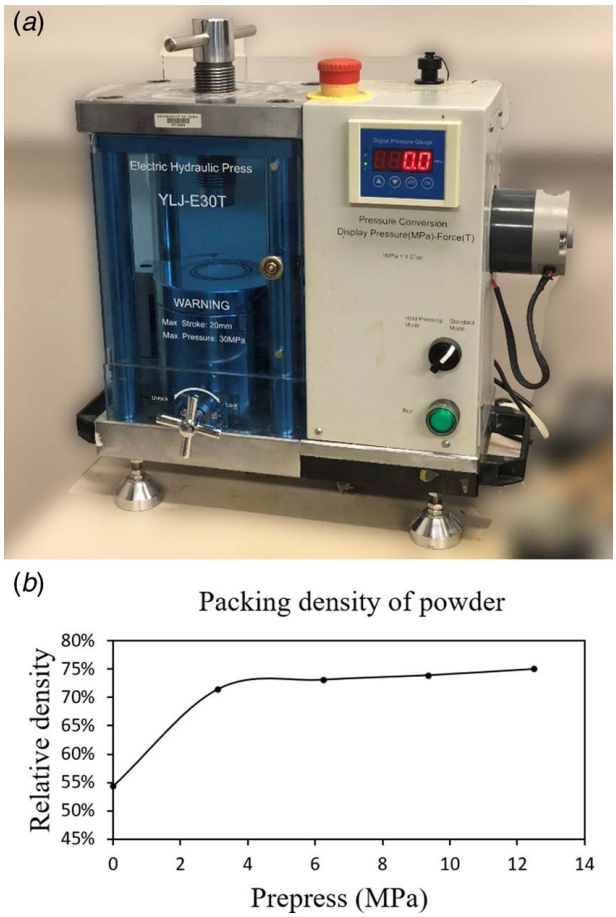

Fig. 8 (*a*) Hydraulic press machine for varying the powder packing density and (*b*) relationship between packing density of powder bed and pre-press pressure

3.2 Diffusion Profiles of Droplet in Powder Bed. Figure 9 shows bonded granules achieved under different pre-press and final press conditions, which were used to approxmite the diffusion profiles of droplets in the powder bed. All the granules were in a shape of a half ellipsoid. The diameters of the bonded granules in top views in Fig. 9 were defined as diffusion width of droplets, and the thicknesses in side views in Fig. 9 were measured as diffusion depth. The diameter and thickness of the bonded granules were measured using a caliper.

The measurement results of diffusion width and depth under different pre-press and final press conditions are shown in Fig. 10. At a fixed final pressure of 0 MPa, a Spearman's correlation was run to assess the association between diffusion depth/width and pre-press using a small sample of 15 measurements. There was a moderate negative association between diffusion depth and pre-press, which was statistically significant, $r_s = -0.655$, $p = 0.008$; there was a strong positive association between diffusion width and pre-press, which was statistically significant, $r_s = 0.797$, $p = 0.000$. When the pre-press increased from 0 to 3.12 MPa, the diffusion width increased dramatically by 74.10%, and the diffusion depth decreased by 30.73%. After the pre-press increased above 3.12 MPa, the diffusion width still slightly increased before reaching a plateau. In contrast, the diffusion depth first decreased and then became relatively stable. These trends are consistent with the change in powder packing density as the pre-press increased from 0 MPa to 12.49 MPa (refer to Fig. 8). This indicates that a higher powder packing density leads to a reduced droplet diffusion in the vertical direction and an increased diffusion along the honrizontal plane, which can be explained by the increased resisting force between a droplet and particles inside a highly packed powder bed and an increased capillary force on the surface of the powder bed that facilitates droplet spreading. It can also be seen that the diffusion depth decreased significantly after the pre-press increased

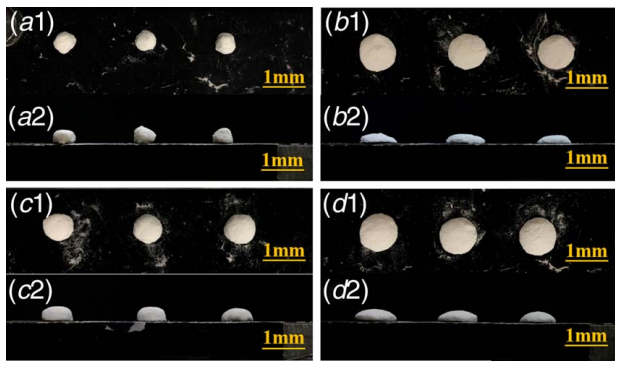

Fig. 9 Experimental results of bonded granules: (*a*1) top view and (*a*2) side view under a pre-press of 0 MPa and a final press of 0 MPa; (*b*1) top view and (*b*2) side view under a pre-press of 12.49 MPa and a final press of 0 MPa; (*c*1) top view and (*c*2) side view under a pre-press of 0 MPa and a final press of 12.49 MPa; (*d*1) top view and (*d*2) side view under a pre-press of 12.49 MPa and a final press of 12.49 MPa

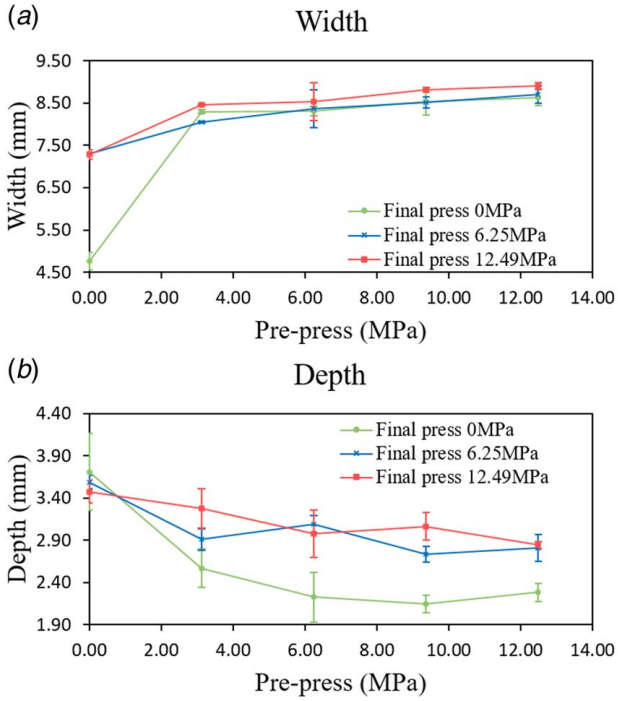

Fig. 10 (*a*) Width and (*b*) depth of diffusion in the powder bed under different pre-press and final pressures

above 3.12 MPa, even though the powder packing density did not change obviously. This may be caused by the nonuniform powder packing along the depth in the powder bed. That is, the powder packing density in the depth direction may be less than that on the surface of powder bed. Further analysis about the relationship between the diffusion and packing density is made in Sec. 3.3.

Figure 10 also shows the diffusion results under final pressures of 6.25 and 12.49 MPa. Similarly, a Spearman's correlation was run to assess the association between diffusion depth/width and pre-press under those two final press. A moderate negative association between diffusion depth and pre-press was found for final press of 6.25 ($r_s = -0.705$, $p = 0.003$) and 12.49 MPa ($r_s = -0.687$, $p = 0.005$); a very strong positive association between diffusion depth and pre-press was found for final press of 6.25 ($r_s = 0.847$, $p = 0.000$) and 12.49 MPa ($r_s = 0.908$, $p = 0.000$). When no pre-press was applied, as the final press increased from 0 to 6.25 MPa, the diffusion width increased dramatically by 53.46% due to the rearrangment diffusion. As the final press continued increasing from 6.26 MPa to 12.49 MPa, the diffusion width stayed the same. This is because the rearrangment diffusion becomes stable after a certain final press, similar to the relationship between the packing density and pre-press in Fig. 8. On the other hand, when the final press increased from 0 to 12.49 MPa, the diffusion depth slightly decreased. Further analysis about the effects of final press on droplet diffusion is detailed in Sec. 3.4.

3.3 Relationship Between Diffusion Profiles and Droplet Depositing Strategies. Figure 11 shows the effects of droplet depositing strategies on the diffusion profile under different pre-press and final press conditions. Similar to the results discussed in Sec. 3.2, a final press of 31.35 kPa leads to an increase in the diffusion width and a decrease in the diffusion depth, in comparison to the results achieved under a final press of 0 kPa. Furthermore, Fig. 11 indicates that the diffusion width of strategy a was always larger than that of dropping strategy b, while the diffusion depth of these two dropping strategies varied depending on the applied pre-press and final press. The difference in the diffusion width may be caused by the interaction of the sequentially deposited

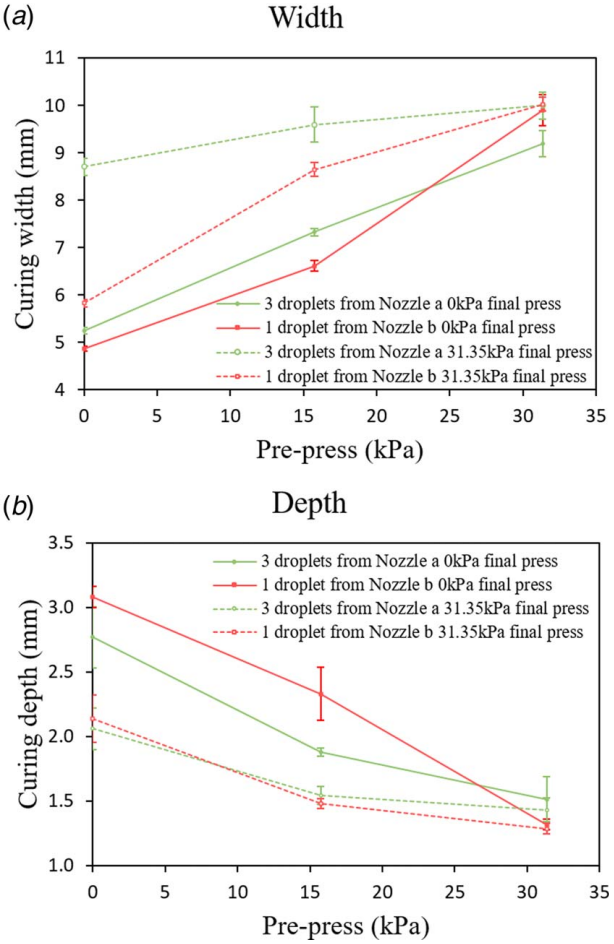

Fig. 11 Diffusion of (*a*) width and (*b*) depth with different droplet sizes

small droplets in the powder bed, whose mechanism requires further study. Discrepancies in the mass of solution or the error of volume measurement for the droplets can also be a possible reason for the difference in diffusion for the study of droplet size. Since strategy b resulted in better control of diffusion width, printing with simultaneous print passes for each layer (strategy b), instead of sequential printing with same passes (strategy a), is preferable for better dimensional control.

3.4 Relationship Between Diffusion Profiles and Packing Density. To quantify the relationship between powder packing density and diffusion profiles, diffusion profiles achieved under different packing densities were simulated in ANSYS FLUENT, as shown in Fig. 12. Since the droplet size in the simulation is different from that used in the experiments, dimensionless depth and width of diffusion are defined as given in Eqs. (12) and (13)

$$d_{dim} = \frac{d_{diff}}{2R_0} \tag{12}$$

$$w_{dim} = \frac{w_{diff}}{2R_0} \tag{13}$$

where d_{diff} and w_{diff} are the diffusion depth and width, and d_{dim} and w_{dim} are the dimensionless depth and width of diffusion. Set the radius of droplet R_0 as 3 mm.

The powder packing densities of the powder bed model used in the simulation were set the same as those achieved in the experiments under different pre-pressing pressures (see Fig. 8) by calculating the distance d_1 between the particles based on Eq. (10).

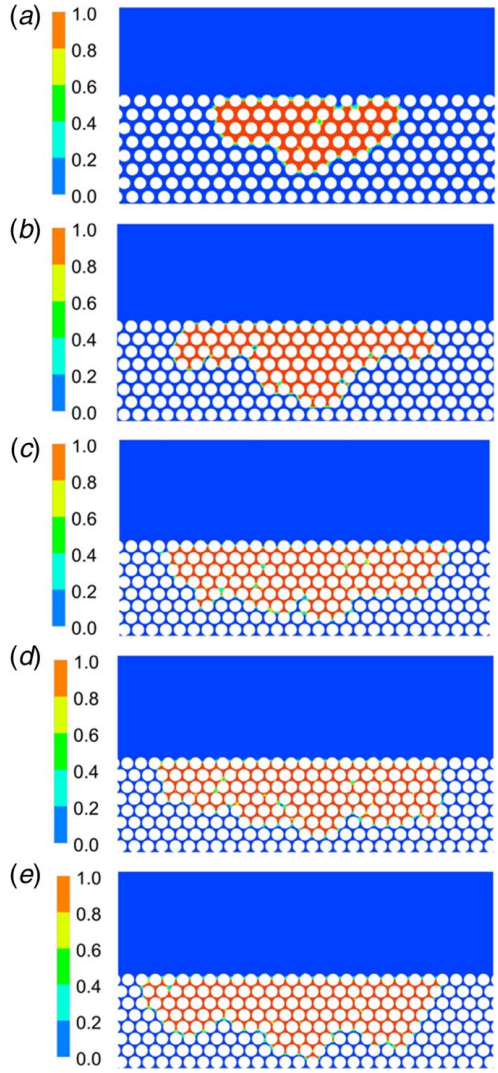

Fig. 12 Simulated diffusion profiles of droplets in powder beds of different packing densities: (*a*) 54.40%, (*b*) 71.49%, (*c*) 73.10%, (*d*) 73.89%, and (*e*) 74.99%

The results are shown in Table 4. The particle diameter d_0 in the simulation was set as 1 mm. The dimensionless width and depth of diffusion under different powder packing densities were calculated from the numerical simulation and compared with the dimensionless diffusion profiles calculated from the experiment results presented in Fig. 10. The calculation results are shown in Fig. 13.

The simulated dimensionless width increased with the increasing packing density, which matches well with the experimental results of the dimensionless width. However, the simulated dimensionless depth increased with the increasing packing density, which shows an opposite trend to the experimental results. A potential reason for this disparity between the simulation and experiments is that the particle arrangement in the simulation is not the same as the actual powder bed in the experiments. That is, in the simulation, all the particles were set with the same distance between each other, and any three neighboring particles were positioned at the vertex of an equilateral triangle; nevertheless, the nanoparticles in the actual powder bed were in close contact with each other with a random arrangement. Further study is required to improve the numerical model for the relationship between droplet diffusion and powder packing density.

Table 4 Distances between the particles in the simulation

Packing density (%)	d_1(mm)
54.40	0.291
71.49	0.184
73.10	0.126
73.89	0.113
74.99	0.108

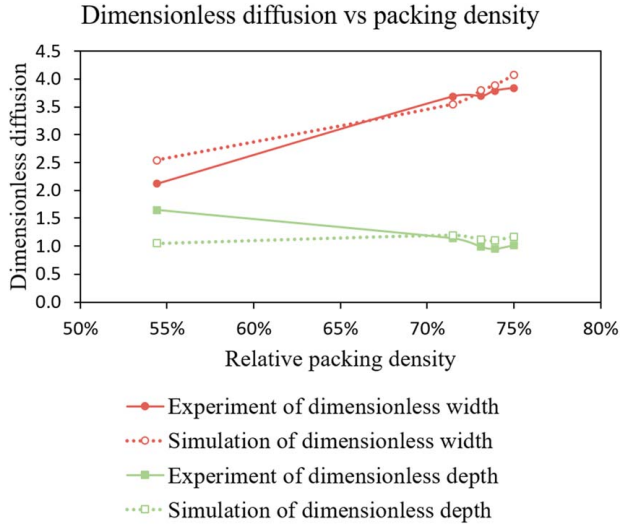

Fig. 13 Dimensionless depth and width of diffusion under different powder packing densities

3.5 Relationship Between Diffusion Profiles and Pressure Difference. The difference between final press p_f and pre-press p_p is defined as

$$\Delta p = p_f - p_p \tag{14}$$

With the same pre-press p_p, the difference between the diffusion width/depth achieved under final press p_f and 0 MPa is defined, respectively, as

$$\Delta w = w_f - w_0 \tag{15}$$

$$\Delta d = d_f - d_0 \tag{16}$$

Based on the results in Fig. 10, the relationship between the diffusion difference $\Delta w/\Delta d$ and the pressure difference Δp is shown in Fig. 14. At a final press of 6.25 MPa, Δw was almost equal to zero when the pressure difference Δp was less than 3.13 MPa. At a final press of 12.49 MPa, Δw was approximately equal to zero when the pressure difference Δp was less than 9.37 MPa. This indicates that when pre-press is greater than 3.12 MPa, the rearrangement diffusion along the horizontal plane (i.e., the width) can be well controlled, regardless of the magnitude of the applied final press (e.g., 6.25 or 12.49 MPa). This is because at a pre-press of 3.12 MPa, the packing density of the powder bed reaches a plateau of around 75%, as shown in Fig. 8. At the final press of 6.25 MPa, Δw increased to 2.55 mm when the pressure difference Δp exceeded 3.13 MPa. At the final press of 12.49 MPa, Δw increased to 2.52 mm when the pressure difference Δp exceeded 9.37 MPa.

At the final press of 6.25 MPa, the diffusion difference Δd in depth was relatively large, when the pressure difference Δp was less than 3.13 MPa. As the pressure difference Δp increased, Δd gradually decreased to a negative value. Similar trend also occurred at the final press of 12.49 MPa. This decrease in the diffusion depth is because a greater pressure difference can directly compress the wet powder compact into a thinner thickness.

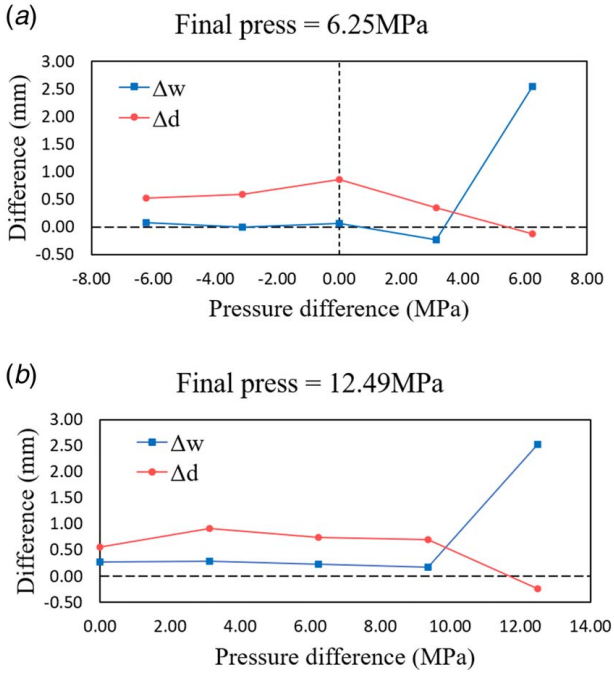

Fig. 14 Relationship between diffusion profile and pressure difference under a final press of (*a*) 6.25 MPa and (*b*) 12.49 MPa

In summary, the droplet diffusion in a powder bed in the HTJF process can be controlled by properly selecting the final press and pre-press. To eliminate the undesired rearrangement diffusion, a critical pre-pressing pressure should be applied to the powder bed at which the packing density can reach a plateau. When a relatively low pre-press pressure is used instead such that the packing density does not reach its highest level, a final press pressure not greater than the pre-press pressure should then be used to mitigate the undesired rearrangement diffusion. In the case of Li_2MoO_4 nanoparticles used in this study, when final press is set as 6.25 MPa or 12.49 MPa, pre-press should be greater than 3.12 MPa.

3.6 Test Cases Printed by HTJF. Using Li_2MoO_4 as the powder and DI water as the ink, two combinations of pre-press and final press were selected to demonstrate their effects on the printing results via the HTJF process, as shown in Table 5. In combination 1, the pre-press was less than the final press, and in combination 2 the pre-press is greater. According to the discussion in Sec. 3.5, combination 2 is able to fabricate parts with higher accuracy because of better control over the diffusion behavior during the HTJF process.

Cross shapes were fabricated using the two combinations of pressures via the HTJF process (see Fig. 15(*a*)). In the process of transient solution deposition (Fig. 1(*a*)), the printed layer thickness was set as 220 μm and the total number of layers was 8. Pre-press was applied to each layer first and then 4 print passes using printing strategy b were applied to the pre-pressed layers. In the process of hydrothermal process, the whole powder compact was pressed by a final press, and the temperature was fixed at 120 °C for 20 min (Fig. 1(*b*)). Finally, the powder compact was dried in the oven at 120 °C for 3 h to remove residual water and those unprinted regions were cleaned by needle and ultrasound. Figures 15(*b*) and 15(*c*) show the part fabricated under the pressure combination 1. As can be seen in the figure, over-solidification occurred along the profile (similar to the results in Figs. 2(*b*)–2(*d*)), due to the undesired rearrangement diffusion of the water. In comparison, combination 2 leads to a part with the desired geometry of sharp corners (Figs. 15(*d*) and 15(*e*)), by which the rearrangement diffusion of water was almost eliminated.

Table 5 Methods of pre-press and final press for HTJF process

Combination	Pre-press (MPa)	Final press (MPa)
1	0.14	12.49
2	0.14	0.05

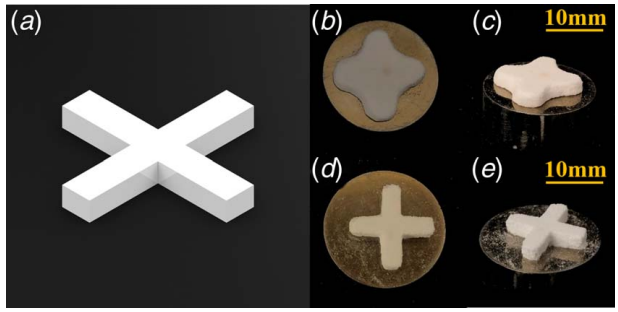

Fig. 15 Fabrication results through the HTJF process under different pre-press and final press: (*a*) CAD model of a cross shape, (*b*) top view and (c) side view of result under pre-press of 0.14 MPa and final press of 12.49 MPa, (*d*) top view and (e) side view of result under pre-press of 0.14 MPa and final press of 0.05 MPa

4 Conclusions and Future Work

The hydrothermal-assisted transient jet fusion process is a new ceramic AM process that utilizes a water-mediated hydrothermal mechanism to fuse particles together. Overcuring is a key issue associated with the HTJF process, which is caused by bad control of water diffusion, in particular rearrangement diffusion, in the process. The water diffusion in the HTJF process is mainly dependent on process parameters, such as powder packing density, final press in hydrothermal fusion, and droplet size. To understand the relationship between the diffusion profiles of water and process parameters, both numerical modeling and experiments were performed. Relationships between diffusion profiles (width and depth) and different process parameters were established. The results indicate that the diffusion in a powder bed in the HTJF process can be controlled by properly selecting final press and pre-press. Future work will be focused on the understanding of mass transport in the HTJF process and the fabrication of complex ceramic structures with high accuracy.

Acknowledgment

This research was funded by the Iowa Technology Institute at the University of Iowa.

Conflict of Interest

There are no conflicts of interest.

Data Availability Statement

The datasets generated and supporting the findings of this article are obtainable from the corresponding author upon reasonable request.

References

[1] Nawaz, M., Sattar, F., and Kundu, S. N., 2019, *Minerals and Rock-Forming Processes, Sustainable Energy and Environment: An Earth System Approach*, Apple Academic Press Inc., Palm Bay, FL, pp. 39–72.

[2] Fei, F., He, L., Zhou, B., Xu, Z., and Song, X., 2019, "Hydrothermal-Assisted Transient Binder Jetting of Ceramics for Achieving High Green Density," JOM, **72**(3), pp. 1–7.
[3] Guo, J., Guo, H., Baker, A. L., Lanagan, M. T., Kupp, E. R., Messing, G. L., and Randall, C. A., 2016, "Cold Sintering: A Paradigm Shift for Processing and Integration of Ceramics," Angew. Chem., Int. Ed., **55**(38), pp. 11457–11461.
[4] Guo, H., Bayer, T. J., Guo, J., Baker, A., and Randall, C. A., 2017, "Current Progress and Perspectives of Applying Cold Sintering Process to ZrO_2-Based Ceramics," Scr. Mater., **136**, pp. 141–148.
[5] Guo, H., Guo, J., Baker, A., and Randall, C. A., 2017, "Cold Sintering Process for ZrO_2-Based Ceramics: Significantly Enhanced Densification Evolution in Yttria-Doped ZrO_2," J. Am. Ceram. Soc., **100**(2), pp. 491–495.
[6] Guo, H., Baker, A., Guo, J., and Randall, C. A., 2016, "Protocol for Ultralow-Temperature Ceramic Sintering: An Integration of Nanotechnology and the Cold Sintering Process," ACS Nano, **10**(11), pp. 10606–10614.
[7] Guo, H., Guo, J., Baker, A., and Randall, C. A., 2016, "Hydrothermal-Assisted Cold Sintering Process: A New Guidance for Low-Temperature Ceramic Sintering," ACS Appl. Mater. Interfaces, **8**(32), pp. 20909–20915.
[8] Guo, H., Baker, A., Guo, J., and Randall, C. A., 2016, "Cold Sintering Process: A Novel Technique for Low-Temperature Ceramic Processing of Ferroelectrics," J. Am. Ceram. Soc., **99**(11), pp. 3489–3507.
[9] Manogharan, G., Kioko, M., and Linkous, C., 2015, "Binder Jetting: A Novel Solid Oxide Fuel-Cell Fabrication Process and Evaluation," JOM, **67**(3), pp. 660–667.
[10] Shahzad, K., Deckers, J., Zhang, Z., Kruth, J.-P., and Vleugels, J., 2014, "Additive Manufacturing of Zirconia Parts by Indirect Selective Laser Sintering," J. Eur. Ceram. Soc., **34**(1), pp. 81–89.
[11] Subramanian, K., Vail, N., Barlow, J., and Marcus, H., 1995, "Selective Laser Sintering of Alumina With Polymer Binders," Rapid Prototyp. J., **1**(2), pp. 24–35.
[12] He, L., Fei, F., Wang, W., and Song, X., 2019, "Support-Free Ceramic Stereolithography of Complex Overhanging Structures Based on an Elasto-Viscoplastic Suspensio," ACS Appl. Mater. Inter., **11**(20), pp. 18849–18857.
[13] He, L., and Song, X., 2018, "Supportability of a High-Yield-Stress Slurry in a New Stereolithography-Based Ceramic Fabrication Process," JOM, **70**(3), pp. 407–412.
[14] Griffith, M. L., and Halloran, J. W., 1996, "Freeform Fabrication of Ceramics via Stereolithography," J. Am. Ceram. Soc., **79**(10), pp. 2601–2608.
[15] Moon, J., Grau, J. E., Knezevic, V., Cima, M. J., and Sachs, E. M., 2002, "Ink-Jet Printing of Binders for Ceramic Components," J. Am. Ceram. Soc., **85**(4), pp. 755–762.
[16] Gonzalez, J., Mireles, J., Lin, Y., and Wicker, R. B., 2016, "Characterization of Ceramic Components Fabricated Using Binder Jetting Additive Manufacturing Technology," Ceram. Int., **42**(9), pp. 10559–10564.
[17] Do, T., Kwon, P., and Shin, C. S., 2017, "Process Development Toward Full-Density Stainless Steel Parts With Binder Jetting Printing," Int. J. Mach. Tools Manuf., **121**, pp. 50–60.
[18] Polozov, I., Sufiiarov, V., and Shamshurin, A., 2019, "Synthesis of Titanium Orthorhombic Alloy Using Binder Jetting Additive Manufacturing," Mater. Lett., **243**, pp. 88–91.
[19] Gaytan, S., Cadena, M., Karim, H., Delfin, D., Lin, Y., Espalin, D., MacDonald, E., and Wicker, R., 2015, "Fabrication of Barium Titanate by Binder Jetting Additive Manufacturing Technology," Ceram. Int., **41**(5), pp. 6610–6619.
[20] Kamaraj, A., Lewis, S., and Sundaram, M., 2016, "Numerical Study of Localized Electrochemical Deposition for Micro Electrochemical Additive Manufacturing," Procedia CIRP, **42**, pp. 788–792.
[21] Liu, Z., Zhang, D., Sing, S., Chua, C., and Loh, L., 2014, "Interfacial Characterization of SLM Parts in Multi-Material Processing: Metallurgical Diffusion Between 316L Stainless Steel and C18400 Copper Alloy," Mater. Charact., **94**, pp. 116–125.
[22] Kähäri, H., Ramachandran, P., Juuti, J., and Jantunen, H., 2017, "Room-Temperature-Densified Li_2MoO_4 Ceramic Patch Antenna and the Effect of Humidity," Int. J. Appl. Ceram. Technol., **14**(1), pp. 50–55.
[23] AAA Molybdenum Products, 2019, "Lithium Molybdate," https://www.aaamolybdenum.com/mo/lithium-molybdate/, Accessed May 18, 2020.
[24] Hosseini, S., 2015, "Droplet Impact and Penetration onto Structured Pore Network Geometries," Doctoral dissertation, University of Toronto.
[25] Tan, H., 2016, "Three-Dimensional Simulation of Micrometer-Sized Droplet Impact and Penetration Into the Powder bed," Chem. Eng. Sci., **153**, pp. 93–107.
[26] Brackbill, J. U., Kothe, D. B., and Zemach, C., 1992, "A Continuum Method for Modeling Surface Tension," J. Comput. Phys., **100**(2), pp. 335–354.
[27] Hirt, C. W., and Nichols, B. D., 1981, "Volume of Fluid (VOF) Method for the Dynamics of Free Boundaries," J. Comput. Phys., **39**(1), pp. 201–225.
[28] Lozano, G. A., von Colbe, J. M. B., Bormann, R., Klassen, T., and Dornheim, M., 2011, "Enhanced Volumetric Hydrogen Density in Sodium Alanate by Compaction," J. Power Sources, **196**(22), pp. 9254–9259.
[29] Wu, C.-Y., Ruddy, O., Bentham, A., Hancock, B., Best, S., and Elliott, J., 2005, "Modelling the Mechanical Behaviour of Pharmaceutical Powders During Compaction," Powder Technol., **152**(1–3), pp. 107–117.